Available online at www.sciencedirect.com
ScienceDirect
Journal of Power Sources 162 (2006) 327–339
JOURNAL OF POWER SOURCES
www.elsevier.com/locate/jpowsour

Effects of channel geometrical configuration and shoulder width on PEMFC performance at high current density

Dewan Hasan Ahmed, Hyung Jin Sung *

Department of Mechanical Engineering, Korea Advanced Institute of Science and Technology, 373-1 Guseong-dong Yuseong-gu, Daejeon 305-701, Republic of Korea

Received 30 May 2006; received in revised form 29 June 2006; accepted 29 June 2006
Available online 10 August 2006

Abstract

Computational fluid dynamics analysis was employed to investigate the performance of proton exchange membrane fuel cells (PEMFCs) with different channel geometries at high operating current densities. A 3D, non-isothermal model was used with a single straight channel geometry. Both anode and cathode humidifications were included in the model. In addition, phase transportation was included in the model to obtain the total water management for systems operating at different current densities. The simulation results showed that a rectangular channel cross-section gave higher cell voltages compared with trapezoidal and parallelogram channel cross-sections. However, the trapezoidal channel cross-section facilitated reactant diffusion, leading to more uniform reactant and local current density distributions over the reacting area, and thus to a lower cathode overpotential of the cell. Simulations of the three different channel cross-sections using the same boundary conditions showed that among the cell geometrical parameters, the shoulder width is one of the most influential in terms of its impact on cell performance. Simulations using different channel–shoulder width ratios showed that at high operating current densities, Ohmic losses significantly increase with decreasing shoulder width. In contrast, a smaller shoulder width facilitates the distribution of reactants and helps to reduce concentration losses. The simulations disclosed the existence of an optimum channel–shoulder width ratio that gives the highest cell voltage under high current density operating conditions. Under such conditions, however, the cell performance deteriorated dramatically with decreasing shoulder width, even when higher reactants flow rates and inlet velocities were used.

Keywords: PEMFC; Geometrical configuration; High current density; Channel–shoulder width ratio; Cathode overpotential; Ohmic loss

1. Introduction

The proton exchange membrane fuel cell (PEMFC) is a promising technology for various applications, including automobiles and stationary power plants. However, PEMFCs require further improvements if they are to be used commercially in the automobile industry, particularly in regard to their power density [1,2]. To obtain high power density, voltage losses of the cell must be minimized and the cell must be operated at high operating current density. It is well established that the major source of voltage loss in PEMFCs is the oxygen reduction reaction (ORR) at the cathode side [3,4]. Furthermore, the water produced at the cathode side leads to concentration losses under high current density operation. Many researchers have highlighted this issue and emphasized the need for optimization of geometrical and physical parameters along with proper water and thermal management. Results obtained using computational fluid dynamic (CFD) analysis have indicated the need to reduce concentration losses in order to improve cell performance [4–10].

Hydrogen and oxygen diffusion through the gas diffusion layer (GDL) and the distributions of these species at the reacting area are also important determinants of fuel cell performance. One of the easiest ways to facilitate the flow of reactants to the reacting area is to change the geometrical configuration of the channel (e.g., length, width, height and shoulder (bipolar plate) width) and the channel flow pattern. A number of studies have endeavored to improve fuel cell performance by varying the channel configuration [8,9,11–17]. It has been suggested that use of a trapezoidal channel cross-section rather than a rectangular or square cross-section may improve the cell performance [18]. Various serpentine flow field designs for both the anode and cathode channels have also been examined to obtain higher output

* Corresponding author. Tel.: +82 42 869 3027; fax: +82 42 869 5027.
E-mail address: hjsung@kaist.ac.kr (H.J. Sung).

0378-7753/$ – see front matter © 2006 Elsevier B.V. All rights reserved.
doi:10.1016/j.jpowsour.2006.06.083

Nomenclature

A_{cv}	specific surface area of the control volume (m^{-1})
$Area_{cv}$	surface area of the control volume (m^2)
C_{wa}	concentration of water vapor at the anode ($mol\,m^{-3}$)
C_{wc}	concentration of water vapor at the cathode ($mol\,m^{-3}$)
$D_{H_2,l}$	diffusion coefficient of H_2 in a liquid water film ($6.3 \times 10^{-9}\,m^2\,s^{-1}$)
$D_{O_2,l}$	diffusion coefficient of O_2 in a liquid water film ($2.4 \times 10^{-9}\,m^2\,s^{-1}$)
D_W	diffusion coefficient of water ($m^2\,s^{-1}$)
F	Faraday constant (96,487 $C\,mol^{-1}$)
h_{rxn}	enthalpy of water formation ($kJ\,K\,mol^{-1}$)
h_{fg}	enthalpy of vaporization of water ($kJ\,kg^{-1}$)
$H_{H_2,l}$	Henry's law constant for H_2 in a liquid water film (8.9×10^9 Pa)
$H_{O_2,l}$	Henry's law constant for O_2 in a liquid water film (2.12×10^{10} Pa)
I	local current density ($A\,m^{-2}$)
I_{avg}	average current density ($A\,m^{-2}$)
$I_{0,K}$	exchange current density for reaction K ($A\,m^{-2}$)
L	length (m)
$M_{m,dry}$	equivalent weight of a dry membrane ($kg\,mol^{-1}$)
M_n	molecular weight of species n ($kg\,mol^{-1}$)
$m_{w,l}$	mass fraction of liquid water
$mass_n$	mass of species n (kg)
n	no. of electrons
n_d	electro-osmosis drag coefficient
$P^{sat}_{w,k}$	saturation vapor pressure of water in stream k (Pa)
P	pressure (Pa)
P_n	partial pressure of species n (Pa)
R	universal gas constant ($8.314\,J\,(mol\,K)^{-1}$)
r	condensation rate (s^{-1})
S	source term
t_f	liquid water film thickness (m)
t_m	membrane thickness (m)
T	temperature (K)
V	velocity ($m\,s^{-1}$)
V_{cell}	cell voltage (V)
V_{OC}	open circuit voltage (V)
W	width (m)
$X_{i,k}$	mole fraction of species i in stream k

Greek letters

α	net water flux per proton
β	permeability (m^2)
ε	porosity of the gas diffusion layer
η	overpotential (V)
λ	water content in the membrane
μ	dynamic viscosity ($kg\,s\,m^{-2}$)
$\rho_{m,dry}$	density of a dry membrane ($kg\,m^{-3}$)
ρ	density of the mixture ($kg\,m^{-3}$)
σ_m	membrane conductivity ($S\,m^{-1}$)
ξ	stoichiometric rate

Subscripts and superscripts

a	anode
c	cathode
ch	channel
cv	control volume
e	electrochemical reaction
glif	gas liquid interface
H_2	hydrogen
k	anode or cathode
l	liquid
O_2	oxygen
reac	reacting
sat	saturated
v	vapor
ξ	dummy variable for direction x, y or z

from PEMFCs [19–27]. All researchers have focused on achieving a uniform reaction over the reacting area by facilitating the distribution of oxygen in the reacting area. Under high operating current density conditions, however, oxygen molecules struggle to reach the reacting area, especially in the downstream portion of the channel.

In PEMFCs, the cell performance also depends on various physical and electrochemical parameters. Recently, Tao et al. [28] and Min et al. [29] examined the parameter sensitivity (11 parameters) of a PEMFC in a 3D, non-isothermal model. In these simulations, the parameters were linked so as to reflect the situation in real PEMFCs; this meant that a variation of one parameter that had a positive influence on cell performance could lead to variations in other parameters that negatively affected the performance [29]. These studies showed that PEMFC performance was sensitive to variations in the transfer coefficient, exchange current density, water vapor diffusion coefficient, oxygen diffusion coefficient, GDL porosity and membrane conductivity. However, other parameters, such as the stoichiometric rate, pressure and temperature, also influenced the fuel cell performance [8,15,30,31], especially the diffusion of reactants to the reacting area. From a geometrical standpoint, the shoulder (bipolar plate) and channel configurations also influence the flow of reactants and have a marked effect on fuel cell performance. Moreover, these geometrical parameters also affect the inlet velocity at the anode and cathode [32–34]. Usually the inlet velocities of the reactants into the channels are defined by the following equation:

$$V_{in,K} = \frac{\xi_k I_{avg} R T_k}{n F P X_i} \frac{A_{reac}}{A_{ch}} \quad (1)$$

where ξ, I_{avg}, R, T, n, F and P are the stoichiometric rate, average current density, molar gas constant, temperature, number of electron, Faraday's constant and pressure, respectively. X_i is the mole fraction of species i, A_{reac} and A_{ch} are the reacting area and channel cross-sectional area, respectively. The subscript k refers

to anode or cathode. A higher inlet velocity facilitates passage of the reactants to the reacting area and leads to a more uniform reaction in the cell. Many researchers have studied the effects of various channel–shoulder width dimensions on PEMFC performance [8,11–14,16,27]. When modifying the PEMFC configurations like channel width, shoulder width or reacting area lead to change the boundary conditions like reactants' inlet velocities or mass flow rates. However, most researchers have either not reported the inlet velocities and flow rates of the respective channels or have not adequately defined the boundary conditions for each cases. In a study of channel size effects using a 2D isothermal model, in which the channel–shoulder width ratio was maintained constant (while varying both the channel and shoulder size), Guvelioglu and Stenger [13] found that cell performance was superior in systems with smaller channel and shoulder sizes. Natarajan and Nguyen [8] and Lin and Nguyen [12] used a 2D model to study the effect on cell performance of a variety of parameters; specifically, they examined the effects on a cell with a given membrane width of varying the number of channels and shoulders while maintaining a constant channel–shoulder width ratio, and also of varying the channel–shoulder width ratio. They found that oxygen and liquid water were transported over the shoulder area more easily in configurations with smaller shoulder widths, leading to enhanced cell performance. Lum and McGuirk [14] and Sun et al. [16] studied the effect of shoulder width on fuel cell performance in 2D and 3D models, respectively, by varying the shoulder width while maintaining a constant channel width. They showed that for systems with smaller shoulder widths, more oxygen diffuses to the catalyst layer through the GDL because of the shorter distance and that water transportation is improved. Moreover, their results indicated that the local current density distribution is significantly improved by decreasing the shoulder width. Recently, Chiang and Chu [17] conducted numerical simulations of a 3D isothermal model of a PEMFC for various channel configurations (channel length, height and shoulder width), with particular emphasis on the effect of channel height on cell performance. They carried out simulations with different combinations of channel width and height while maintaining the same channel cross-sectional area and constant flow rate. Their results indicated that flat channels (i.e., smaller height) gave better performance.

In the present study, we performed simulations to investigate the performance of PEMFCs at high operating current density for various channel cross-sectional configurations, while maintaining the same reactant flow rates and inlet boundary conditions. In addition, we examined the different types of voltage losses of the cell with related water and thermal management at high operating current density. Emphasis was placed on examining the effect of varying the channel–shoulder width ratio for a given channel height under high current density operation. Particular attention was given to investigating the cell performance with the model boundary conditions governed by Eq. (1) and also to maintain the same boundary conditions for different channel–shoulder width ratios. For each geometrical configuration, the cell performance was investigated in detail by examining the reactants, local current density, membrane conductivity, anode and cathode overpotentials, and water and thermal management. A 3D model with a single straight channel geometry was used for the computational analysis. The simulation results were validated by comparison with results in the literature.

2. Numerical simulation

Schematic diagrams of the computational domain and its cross-sectional view are shown in Fig. 1. The system consists of two channels (for hydrogen and air) between which the membrane electrode assembly (MEA) is sandwiched. There are bipolar plates (also known as shoulders) on both the anode and cathode sides, which function as current collectors with high electronic conductivity. Humidified hydrogen and air are introduced into the respective channels in quantities determined by the stoichiometric rate and average current density. The following assumptions are made in the model: ideal gas mixture, steady state, laminar flow, isotropic and homogeneous porous gas diffusion layer, homogeneous two phase flow and negligible potential drop in the bipolar plates.

The governing equations for the numerical simulation are conservation of mass, momentum transport, species transport and energy equations.

Conservation of mass equation:

$$\nabla \cdot (\rho \vec{u}) = S_{m_a} + S_{m_c} \tag{2}$$

The source terms are

$$S_{m_a} = S_{H_2} + S_{wv_p} + S_{wl_p} + S_{awv_e}, \tag{2.1}$$

$$S_{m_c} = S_{O_2} + S_{wv_p} + S_{wl_p} + S_{cwv_e}, \tag{2.2}$$

where

$$S_{H_2} = -\frac{M_{H_2} A_{cv} I}{2F} \quad \text{and} \quad S_{O_2} = -\frac{M_{O_2} A_{cv} I}{4F}. \tag{2.3}$$

The mass contributions of the water vapor at the anode and cathode sides are

$$S_{awv_e} = -\frac{M_{H_2O} A_{cv} \alpha I}{F}, \tag{2.4}$$

$$S_{cwv_e} = S_{cwv_t} + S_{cwv_p} = \frac{M_{H_2O} A_{cv} I}{2F} + \frac{\alpha M_{H_2O} A_{cv} I}{F}$$

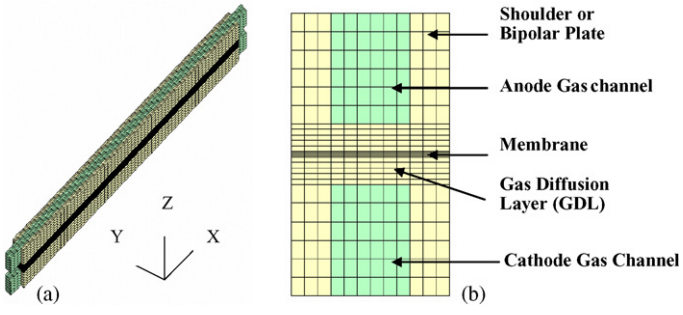

Fig. 1. Single straight channel flow field for a PEMFC. (a) Geometry and (b) cross-sectional view.

$$= \frac{(1+2\alpha)M_{H_2O}A_{cv}I}{2F}. \quad (2.5)$$

The phase change between water vapor and liquid water depends on the partial pressure, and is defined as

$$S_{wl_p} = -S_{wv_p} = -\frac{M_{H_2O}(\sum_{n\,of\,v}\text{mass}_{n\,of\,v}/M_{n\,of\,v})}{(1-(P_{wv}^{sat}/P))} \times \left[\frac{P_{wv}^{sat}-P_{wv}}{P}\right] \times r. \quad (2.6)$$

r is the condensation rate and set as $1\ s^{-1}$ in the model. Eq. (2.6) shows the way of phase change in water by checking the partial pressure of water vapor compared with saturated pressure. If the partial pressure of water vapor is greater than the saturated pressure, this water vapor will condense to liquid water. If the partial pressure of water vapor is lower than the saturated pressure, the liquid water will evaporate to water vapor.

In Eqs. (2.4) and (2.5), α is the net water transfer coefficient per proton through the membrane and defined as

$$\alpha = n_d - \frac{FD_W[C_{wc}-C_{wa}]}{It_m} \quad (2.7)$$

The electro-osmotic drag coefficient (n_d) and water diffusion coefficient (D_W) can be correlated with membrane water content (λ) [35] as follows:

$$n_d = 0.0029\lambda^2 + 0.05\lambda - 3.4\times10^{-19}. \quad (2.8)$$

Momentum transport equation:

$$\nabla\cdot(\rho\vec{u}\vec{u}) = -\nabla P + \nabla\cdot(\mu\nabla\vec{u}) + S_{p,i}. \quad (3)$$

where $S_{p,i}$ is the sink source term for porous media in the x, y and z directions. As the pressure drops in porous media, Darcy's law has taken into account in the model. The source term is defined as

$$S_{p,i} = -\left(\sum_{j=1}^{3}\frac{1}{\beta_j}\mu u_j\right). \quad (3.1)$$

Here, β is the permeability.

General species transport equation:

$$\nabla\cdot(\rho m_n\vec{u}) = \nabla\cdot(J_n) + S_s. \quad (4)$$

where n denotes H_2, O_2, water vapor or liquid water. The source terms are the same as those for the conservation of mass equation. The transportation of the species is solved with bulk mixture velocities and with diffusion mass fluxes. The diffusion mass flux of each species is evaluated with binary diffusion coefficients [36] and is reduced by 50% in the diffusion layer to account for the effect of porosity and tortuosity of the pores [37]. It is assumed that the liquid water is in small droplet forms and freely suspended in the gas flow. This allows that two phases flow together (homogeneous two phase flow) at normal operating conditions for a steady state rather than at supersaturated conditions.

The diffusion mass flux (J) of species n in direction ξ is

$$J_{\xi,n} = -\rho D_{\xi,n}\frac{\partial m_{K,n}}{\partial\xi}, \quad (4.1)$$

where ξ is a dummy variable for direction x, y or z.

Energy equation:

$$\nabla(\rho\vec{u}h) = \nabla\cdot(k\nabla T) + S_h. \quad (5)$$

The source term S_h contains contributions from energy losses and heat associated with phase transformations. The heat source from the electrochemical reaction is given by the difference between the total energy released by the electrochemical reaction at the cathode membrane surface and the electrical energy extracted out of the fuel cell [38]:

$$S_{h_e} = h_{rxn}\left[\frac{IA_{cv}}{2F}\right] - IV_{cell}A_{cv}. \quad (5.1)$$

The heat source due to a phase change can be expressed as

$$S_{h_p} = S_{wl_p}\times h_{fg}, \quad (5.2)$$

where h_{fg} is the enthalpy of formation of water. The local current density of the cell is calculated as follows from the open circuit voltage (V_{OC}) and the losses

$$I = \frac{\sigma_m}{t_m}\{V_{OC} - V_{cell} - \eta\}, \quad (6)$$

which can be rewritten as

$$V_{cell} = V_{OC} - \eta - \frac{t_m}{\sigma_m}I \quad (7)$$

The last term on the right hand side of Eq. (7) corresponds to the Ohmic loss, where t_m is the membrane thickness and σ_m is the membrane conductivity, both of which are calculated as functions of the water content on the membrane surface at the anode interface. The membrane conductivity can be defined as

$$\sigma_m = \left(0.514\frac{M_{m,dry}}{\rho_{m,dry}}C_{wa} - 0.326\right)\exp\left(1268\left(\frac{1}{T_0}-\frac{1}{T}\right)\right), \quad (8)$$

where $T_0 = 303$ K. The water vapor concentration is defined as

$$C_{w,a} = \frac{\rho_{m,dry}}{M_{m,dry}}\lambda. \quad (9)$$

where $\rho_{m,dry}$ and $M_{m,dry}$ are the material density and the equivalent weight of a dry PEM, respectively. Water content in the membrane (λ) is defined as

$$\begin{aligned} &\lambda = 0.043 + 17.8a_K - 39.8a_K^2 + 36.0a_K^3, && \text{if} \quad a_K \le 1 \\ &\lambda = 14 + 1.4(a_K - 1), && \text{if} \quad a_K > 1 \end{aligned} \quad (10)$$

The subscript K stands for anode or cathode. a_a is the water activity and defined as

$$a_a = \frac{X_{w,a}P}{P_{w,a}^{sat}}. \quad (11)$$

where P is the cell pressure and $X_{w,a}$ is the mole fraction of water on anode side.

The local overpotential (η) for a PEMFC is included for both the anode overpotential (aop) and cathode overpotential (cop),

and can be written as

$$\eta = \frac{RT}{\alpha_c F} \ln\left[\frac{IP}{I_{0_{O_2}} P_{0_{O_2}}}\right] + \frac{RT}{\alpha_a F} \ln\left[\frac{IP}{I_{0_{H_2}} P_{0_{H_2}}}\right], \quad (12)$$

where P is the pressure and P_0 is the partial pressure of the reactants, α_a and α_c are the transfer coefficients for the anode and cathode, respectively, and I_0 is the exchange current density. The partial pressure is calculated as $P_{O_2} = X_{O_2} P$, and $P_{H_2} = X_{H_2} P$. Here X_{O_2} and X_{H_2} are the oxygen and hydrogen mole fraction, respectively. By including the partial pressure, the overpotential terms also include the activation and concentration overpotentials.

The mole fraction of each species used in these model equations is extrapolated to the membrane surface by linear extrapolation, except when a liquid water film is generated on the membrane surface. In this latter case, Henry's Law was used to calculate the solubility of reactants in the liquid water film [38]:

$$-\frac{I}{4F} M_{O_2} = \rho_{O_2} D_{O_2,l} \left[\frac{X_{O_2,glf} P_{glf} H_{O_2,l}^{-1} - X_{O_2}}{t_{f,c}}\right],$$
$$-\frac{I}{2F} M_{H_2} = \rho_{H_2} D_{H_2,l} \left[\frac{X_{H_2,glf} P_{glf} H_{H_2,l}^{-1} - X_{H_2}}{t_{f,a}}\right] \quad (13)$$

where P_{glf} is the pressure at the gas–liquid water interface, H the Henry constant of the reactants in the liquid water film and $t_{f,K}$ is the liquid water film thickness for the anode and cathode, which is defined as

$$t_{f,K} = \frac{m_{w,l}(\sum \text{mass}_n)}{\varepsilon \rho_{wl} \text{Area}_{cv}}. \quad (14)$$

where ε is the porosity of the GDL and mass_n is the mass of species n.

The above all governing equations and appropriate boundary conditions were solved by using the user coding capabilities of STAR-CD that employ a finite volume method.

3. Results and discussion

A series of simulations were carried out on the base case from low operating current density to high operating current density; the geometrical and physical parameters for the base case are shown in Tables 1 and 2, respectively. The polarization curve for the base case, shown in Fig. 2a, shows three distinct regions of losses. The variations in the different overpotentials as a function of operating current density, shown in Fig. 2b, also follow the typical trend found in the literature [29,39,40]. It should be noted that the Ohmic loss in Fig. 2b shows a non-linear trend rather than the linear trend reported in literature because the present model was implemented with variable membrane conductivity.

Table 1
Geometrical parameters

Parameter	Value
Channel length (mm)	34.7
Channel width (mm)	1
Channel height (mm)	1
Membrane length (mm)	31.7
Membrane thickness (mm)	0.05
Anode gas diffusion layer (mm)	0.25
Cathode gas diffusion layer (mm)	0.25

Table 2
Physical and electrochemical parameters

Parameter	Value
Anode pressure (atm)	1
Cathode pressure (atm)	1
Stoichiometric rate at anode	1.2
Stoichiometric rate at cathode	2.0
Cell temperature (°C)	70
Anode inlet temperature (°C)	80
Cathode inlet temperature (°C)	70
Open circuit voltage (V)	0.96
Relative humidity at anode (%)	100
Relative humidity at cathode (%)	100
Oxygen inlet mole fraction	0.143
Oxygen exchange current density ($A\,m^{-2}$)	200
Hydrogen exchange current density ($A\,m^{-2}$)	2000
Anode transfer coefficient	1.2
Cathode transfer coefficient	0.6
Porosity	0.7
Permeability (m^2)	1×10^{-12}
Anode top surface temperature (z-direction) (°C)	70
Cathode top surface temperature (z-direction) (°C)	70

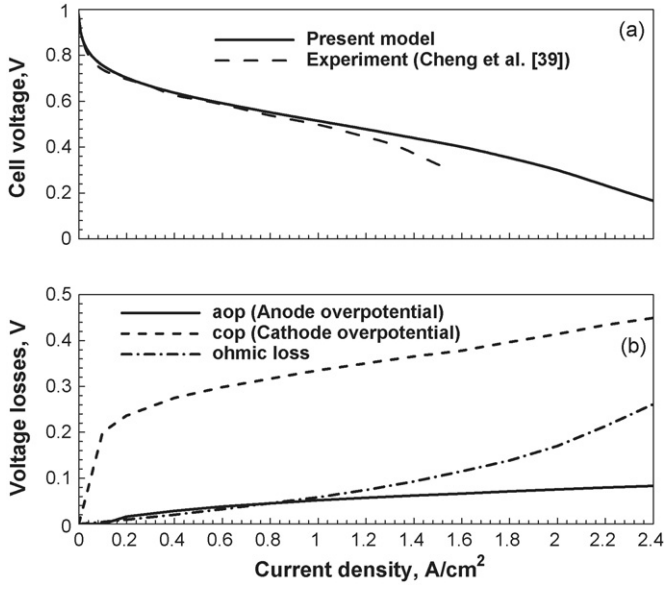

Fig. 2. (a) Polarization curve and (b) different types of voltage loss.

3.1. Effect of channel cross-section and shoulder width

In this study, PEMFC configurations with three channel cross-sections (rectangular, trapezoidal and parallelogram) and different shoulder widths were used. Cross-sectional views of these channel geometries are shown in Fig. 3, and the geometrical parameters of the configurations used are listed in Table 3. The same channel cross-sectional area was maintained, which ensured the same reactant flow rate and inlet boundary con-

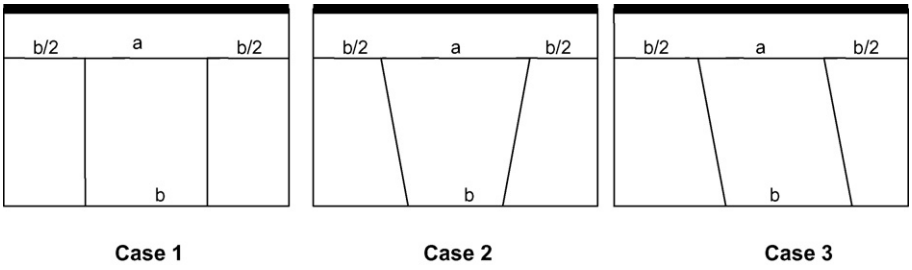

Fig. 3. Cross-sectional view of different geometrical configurations.

ditions for the three cases. To accentuate any differences in cell performance among the different channel cross-sections, a high average current density was chosen. The output voltages at the high operating current density of $I_{avg} = 2.4\ A\ cm^{-2}$ are shown in Fig. 4a for the three cases. The cell voltage for Case 1 (the base case) is slightly higher than those for the other two cases. Case 2, which has a smaller shoulder width (half shoulder width = 0.35 mm) exhibits a lower cell voltage at this high operating current density. To ascertain the real scenario of the cell performance, different cell voltage losses (width average) at the membrane–GDL interface were calculated at the inlet and exit regions of the channel (Fig. 4b and c, respectively). According to Eq. (7), the cell voltage is obtained by subtracting the losses from the open circuit voltage. The losses consist of the aop, cop [aop and cop were already defined above] and Ohmic loss. Fig. 4b and c shows that for all cases, the aop maintains a constant value of approximately 0.08 V along the entire channel length, consistent with previous findings that the aop is negligible in hydrogen fuel cells [3]. By contrast, the cop and Ohmic loss account for around 90% of the total losses. We therefore concentrate on analyzing the Ohmic loss and cop in detail in the following sections.

Table 3
Geometrical configurations

Case	Channel width (mm)	Half shoulder width (mm)	Channel height (mm)	Reacting area (cm^2)
Case 1	0.8	0.4	1	0.5076
Case 2	0.9	0.35	1	0.5076
Case 3	0.8	0.4	1	0.5076

3.1.1. Ohmic loss

According to Eq. (7), the Ohmic loss is directly proportional to the membrane thickness (t_m) and local current density (I) and inversely proportional to the membrane conductivity (σ_m).

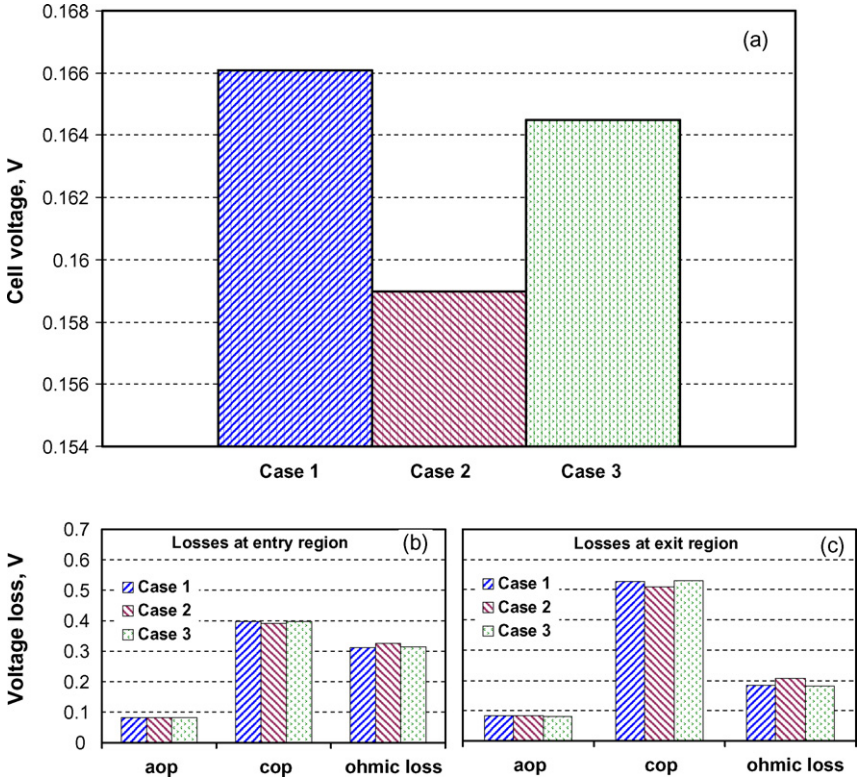

Fig. 4. (a) Cell voltage obtained for different cases ($I_{avg} = 2.4\ A\ cm^{-2}$), (b) voltage losses at $L/L_0 = 0.043$ (entry region) and (c) voltage losses at $L/L_0 = 0.957$ (exit region).

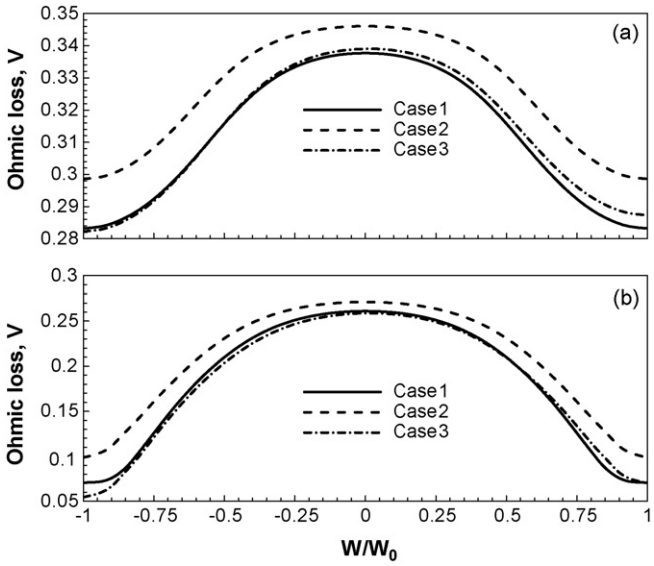

Fig. 5. Comparison of Ohmic losses at the membrane–cathode GDL interface. (a) $L/L_0 = 0.043$ (entry region) and (b) $L/L_0 = 0.957$ (exit region).

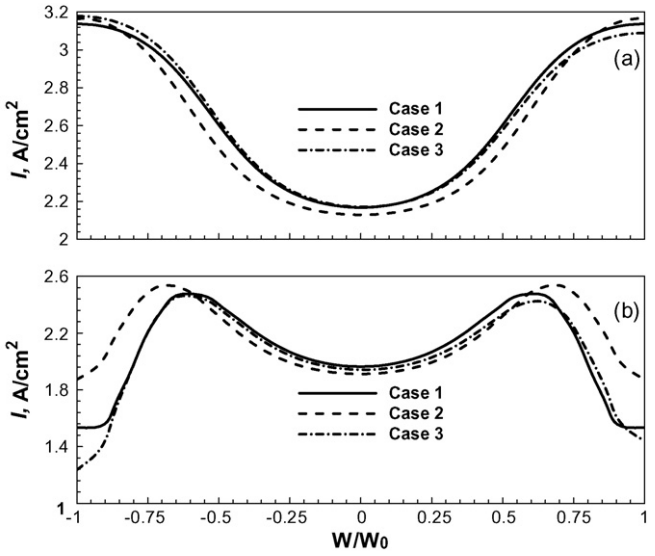

Fig. 7. Comparison of local current density at the membrane–cathode GDL interface. (a) $L/L_0 = 0.043$ (entry region) and (b) $L/L_0 = 0.957$ (exit region).

The simulation results indicate that over the reacting area, the Ohmic loss is higher in the channel area than in the shoulder area, and that the Ohmic loss decreases on going from the channel entry to exit (comparing Fig. 5a and b). The reason for these variations in Ohmic loss in the PEMFC can be found in the distributions of membrane conductivity (Fig. 6) and local current density (Fig. 7). The membrane conductivity is the main factor regulating the Ohmic loss in the PEMFC. It is higher in the shoulder area and lower in the channel area; however, it gradually increases along the channel because of variations in the anode water activity and temperature. The distributions of anode water activity and temperature in the inlet and exit regions are shown in Figs. 8 and 9, respectively. The temperature decreases both along the channel and away from the channel center. The temperature variation along the width is due to the fixed temperature and good thermal conductivity of both anode and cathode bipolar plates. The slight temperature decrease along the channel is due to the effects of heat generation from the electrochemical reactions, water evaporation and fixed top surface temperature of both anode and cathode bipolar plates. Usually, the membrane water contents decrease at the beginning of the channel and result to increase the temperature sharply. Further down of the channel, temperature decreases slowly as the membrane water contents increase through the electrochemical reactions [41]. These temperature variations and distributions in Fig. 9 are also consistent with Shimpalee and Dutta [42].

The above comparison shows that the larger channel width and smaller shoulder width of Case 2 (see Table 3) result in a

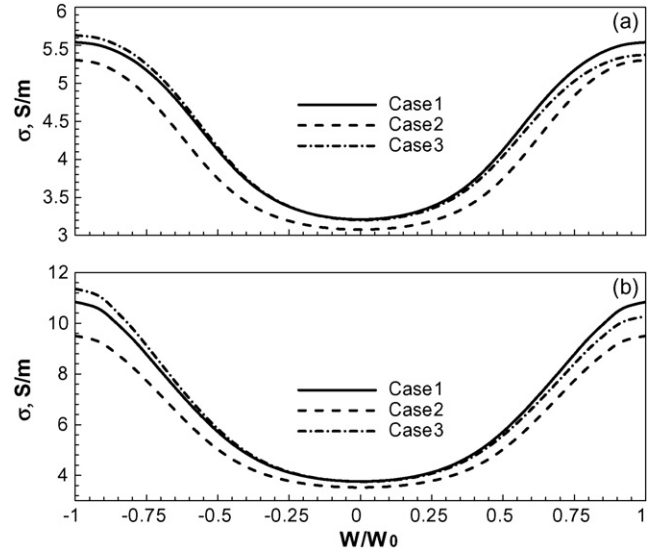

Fig. 6. Comparison of membrane conductivity at the membrane–cathode GDL interface. (a) $L/L_0 = 0.043$ (entry region) and (b) $L/L_0 = 0.957$ (exit region).

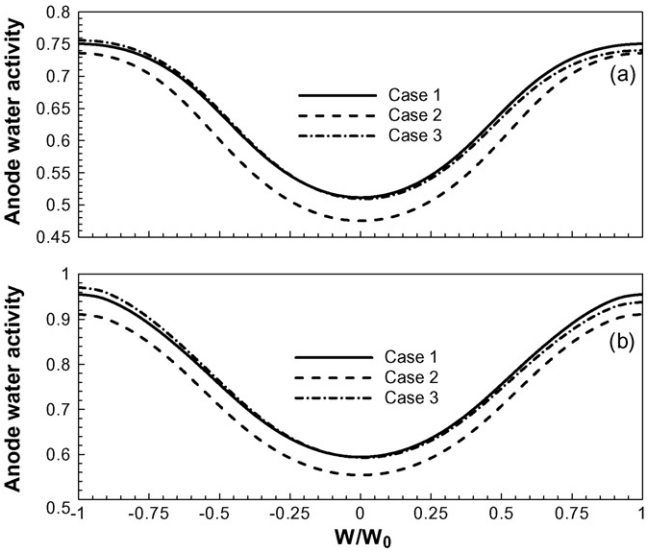

Fig. 8. Comparison of anode water activity at the membrane–anode GDL interface. (a) $L/L_0 = 0.043$ (entry region) and (b) $L/L_0 = 0.957$ (exit region).

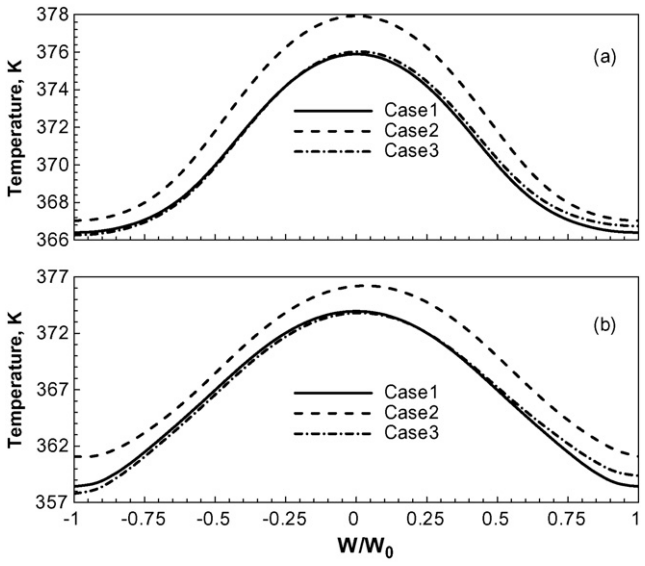

Fig. 9. Comparison of temperature at the membrane–cathode GDL interface. (a) $L/L_0 = 0.043$ (entry region) and (b) $L/L_0 = 0.957$ (exit region).

much more uniform reaction over the reacting area. It is also evident that the temperature at the membrane–cathode GDL interface is higher for Case 2 than for Cases 1 and 3, leading to a reduction in the anode water activity in the cell because the water saturation pressure increases with temperature. However, comparison of Cases 1 and 3, which have the same shoulder and channel widths, indicates that the inclination of the channel walls (Case 3) does not have a significant effect on the water activity and temperature distributions, at this high operating current density.

The results for the Ohmic loss at the membrane–cathode GDL interface for the three cases (Fig. 5) indicate that the configuration with a larger channel width and smaller shoulder width (Case 2) experienced higher Ohmic losses. The other two cases (Cases 1 and 3), which had the same channel and shoulder widths, showed almost the same Ohmic losses.

3.1.2. Cathode overpotential

Our results show that major losses of the cell voltage occur at the cathode side, with the cop accounting for around 65% of the total losses at the exit region of the channels. Inspection of the cop distribution in the fuel cell, shown in Fig. 10, discloses that the cop increases significantly in the shoulder region as well as in the downstream region of the channels. The loss due to the cop incorporates the activation and concentration losses at the cathode side, which are mainly regulated by oxygen availability at the membrane–cathode GDL interface. The profile of the oxygen mole fraction at the membrane–cathode GDL interface is shown in Fig. 11. Oxygen scarcity in the shoulder region over the reacting area leads to higher concentration losses, which become worse in the downstream region of the channel due to depletion of the reactant with moving downstream. Usually, at high operating current density, more molecules react and hence more water is produced. This results in larger quantities of water at the GDL, which reduces the oxygen diffusivity in the cell. This effect is particularly severe in the shoulder area, where water tends to accumulate.

Among the three cases considered here, Case 2 shows a lower cop in both the channel and shoulder areas. Increasing the channel width (or face to the reacting area), as in Case 2, facilitates the diffusion of the reactants to the reacting area. For this case, the cop is much lower at the shoulder region than for the other two cases (Figs. 10 and 11). However, Cases 1 and 3 exhibit similar oxygen mole fractions and cathode overpotentials because they have the same shoulder width.

In the cell with the trapezoidal cross-section (Case 2), the reactants diffused more uniformly, which helped to reduce the concentration losses and to obtain a more uniform local current distribution over the reacting area (see Fig. 7). In the trapezoidal channel configuration of Case 2, however, the shoulder

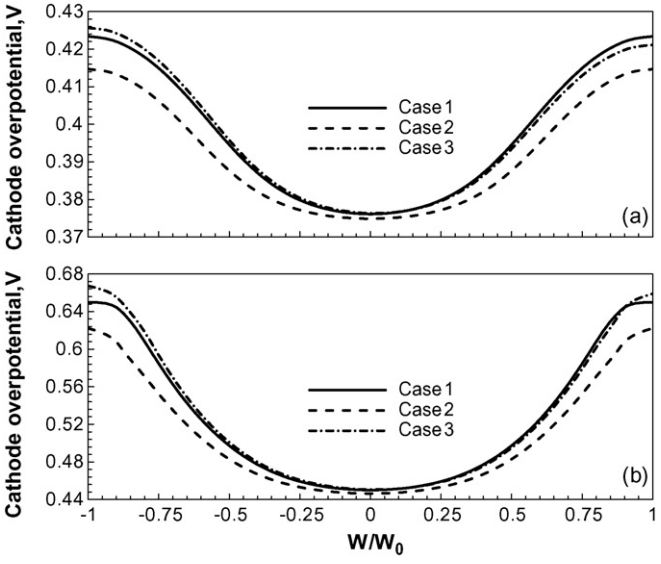

Fig. 10. Comparison of cathode overpotential at the membrane–cathode GDL interface. (a) $L/L_0 = 0.043$ (entry region) and (b) $L/L_0 = 0.957$ (exit region).

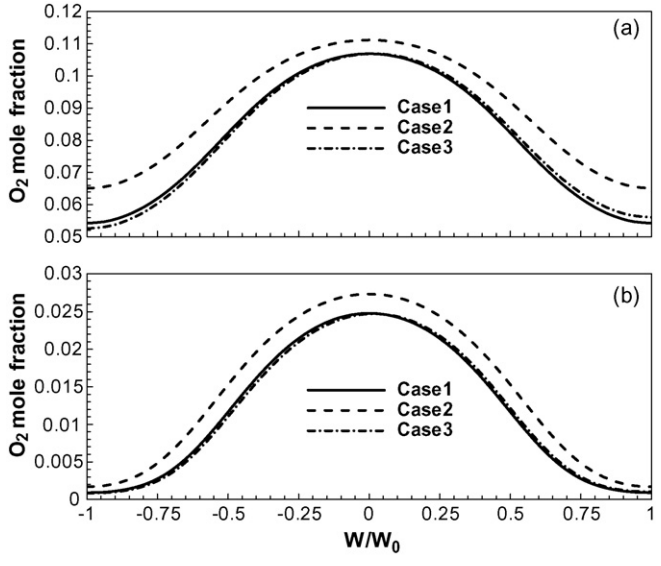

Fig. 11. Comparison of O_2 mole fraction at the membrane–cathode GDL interface. (a) $L/L_0 = 0.043$ (entry region) and (b) $L/L_0 = 0.957$ (exit region).

Table 4
Geometrical configurations for the shoulder width case studies

Case	Sub case	Ch:Sh	Half shoulder width (mm)	Channel width (mm)	Channel height (mm)	Reacting area (cm^2)
Case 4	Case 4.1	1:1	0.4	0.8	1	0.5076
	Case 4.2	1.33:1	0.3	0.8	1	0.4442
	Case 4.3	2:1	0.2	0.8	1	0.3807
	Case 4.4	4:1	0.1	0.8	1	0.3173
Case 5[a]	Case 5.1	1:1	0.4	0.8	1	0.5076
	Case 5.2	1.33:1	0.3	0.8	1	0.4442
	Case 5.3	2:1	0.2	0.8	1	0.3807
	Case 5.4	4:1	0.1	0.8	1	0.3173

[a] Boundary conditions (velocity and mass flow rate at anode and cathode inlet) for Case 5 were maintained constant at the same values as for Case 4.1.

width was reduced to maintain the same channel cross-sectional area as for Cases 1 and 3, which led to significantly increased Ohmic losses, especially in the shoulder area. The results of the present study of three channel geometries indicate that the shoulder width is one of the major geometrical parameters regulating voltage losses. Hence, we continued our study by examining the behavior of cells with a rectangular channel cross-section, as in Case 1, but with different shoulder widths.

In our investigation of systems with rectangular channel cross-sections, we simulated our model in two different ways. The geometrical parameters for these studies are shown in Table 4. For Cases 4.1–4.4, the inlet boundary conditions were set as in Eq. (1), and the shoulder width was varied. For Cases 5.1–5.4, however, all of the models were simulated using the same boundary conditions as for Case 1 (i.e., reactant flow rates and inlet velocities) but with different shoulder widths. As a result, the Case 5 configurations with smaller shoulder widths have higher reactant flow rates and inlet velocities than for Case 4.

3.2. Channel–shoulder width ratio

To study the effect of the channel–shoulder width ratio on PEMFC performance, we carried out simulations for different range of current densities like low, moderate high and high current densities. It should be noted that in these simulations we kept the channel width constant and reduced the shoulder width. Here, Case 4.1 is the same as Case 1 and Cases 4.2, 4.3 and 4.4 have channel–shoulder width ratios of 1.33, 2 and 4, respectively. The cell voltages obtained for current densities of $I_{avg} = 2.4$, 1.6 and 0.6 A cm^{-2} are shown in Fig. 12a. The cell voltage for the operating current density of 0.6 A cm^{-2} is almost independent of the channel–shoulder width ratio. For the other two operating current densities, however, the cell voltage varies with increasing channel–shoulder width ratio. Fig. 12b and c shows the cell voltage as a function of channel–shoulder width ratio for $I_{avg} = 2.4$ and 1.6 A cm^{-2}, respectively, with a smaller voltage scale. It is evident in Fig. 12b and c that the cell voltage goes through a maximum as the channel–shoulder width ratio is increased,

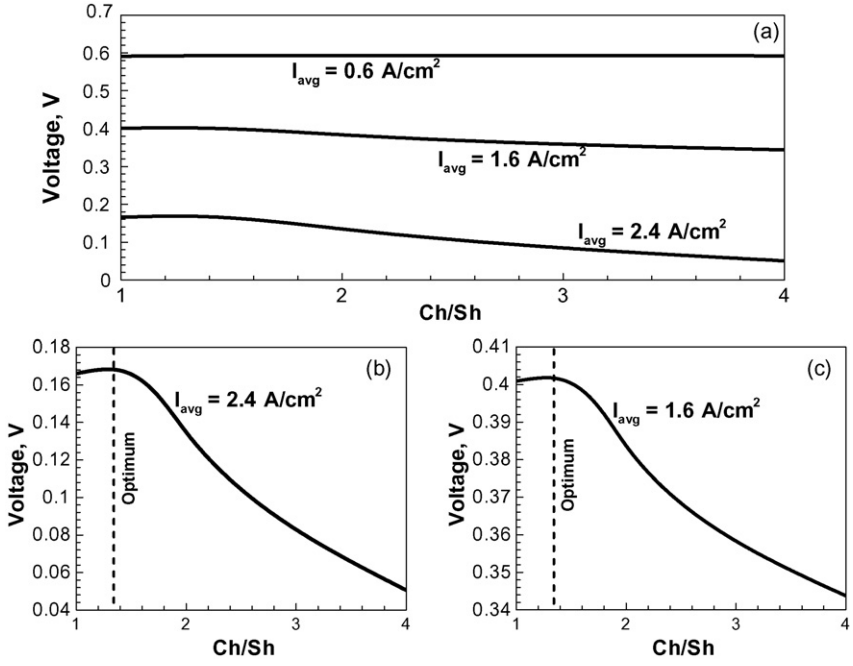

Fig. 12. Comparison of cell voltages for different channel–shoulder width ratios. (a) At different operating current densities, (b) $I_{avg} = 2.4$ A cm^{-2} and (c) $I_{avg} = 1.6$ A cm^{-2}.

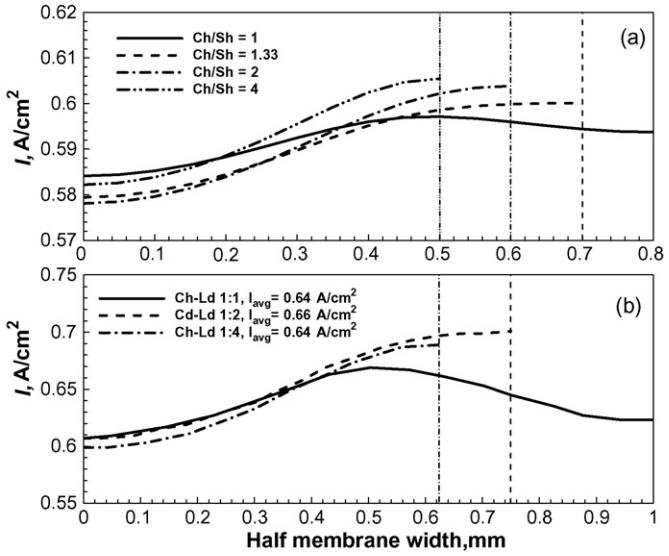

Fig. 13. Comparison of local current density distribution for different channel–shoulder width ratios. (a) Present study for $I_{avg} = 0.6\ A\ cm^{-2}$ at $L/L_0 = 0.5$ and (b) Sun et al. [16].

indicating that there exists an optimum channel–shoulder width ratio of Ch/Sh = 1.3–1.4 at high operating current density. However, the cell performance decreases significantly for higher operating current density with higher channel–shoulder width ratio. Fig. 13a shows the local current density distribution (half channel and half shoulder) for different channel–shoulder width ratios for the operating current density of $0.6\ A\ cm^{-2}$ at $L/L_0 = 0.5$. Similar trends of the local current density profile were observed by Sun et al. [16] for operation at an average current density of around $0.65\ A\ cm^{-2}$. For Ch/Sh = 1, the maximum local current density at the channel–cathode GDL interface is just above the channel–shoulder interface (Fig. 13a and b). On increasing the channel–shoulder width ratio, however, the maximum local current density shifts towards the shoulder region.

The different voltage losses (aop, cop and Ohmic loss) at the inlet and exit regions for systems with channel–shoulder width ratios of 1, 1.33, 2 and 4, operating at high current density ($I_{avg} = 2.4\ A\ cm^{-2}$), are shown in Fig. 14. It is clear that the cop and Ohmic loss gradually increase and decrease along the channel, respectively, for all of the channel–shoulder width ratios. At both the inlet and exit regions, the Ohmic loss increases significantly with increasing channel–shoulder ratio. By contrast, the cop gradually decreases with increasing channel–shoulder width ratio up to Ch/Sh = 2, and then remains almost unchanged on further increase to Ch/Sh = 4. Examination of the local current density distributions for the systems with Ch/Sh = 1, 1.33, 2 and 4 at the inlet and exit regions (Fig. 15a and b, respectively) reveals some interesting behavior. In the exit region (Fig. 15b), the local current density distribution over the membrane–cathode GDL interface is more uniform for higher channel–shoulder width ratios. In the shoulder area, the local current density is also improved at higher channel–shoulder width ratios, however, the local current density at Ch/Sh = 4 is not increased at the shoulder area compared with Ch/Sh = 2.

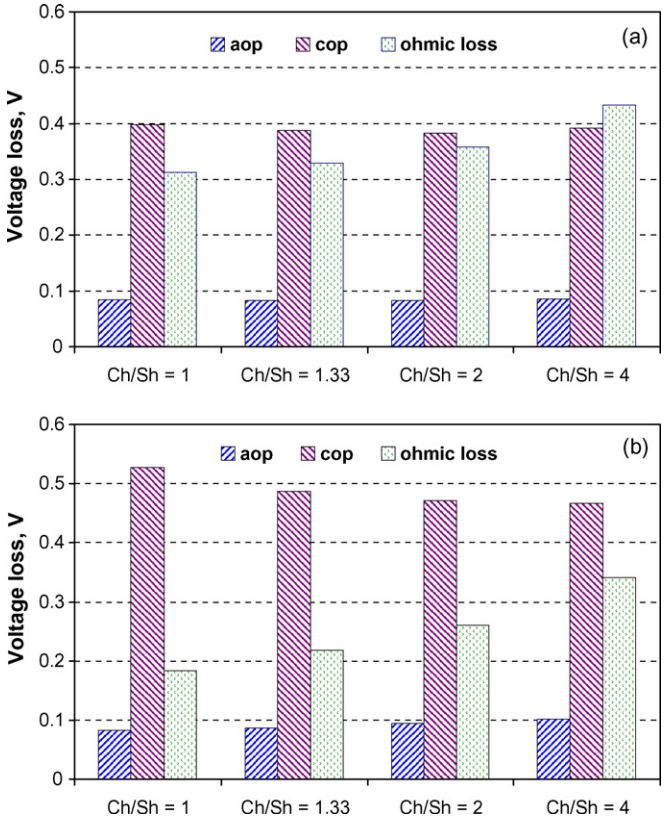

Fig. 14. Comparison of different voltage losses for $I_{avg} = 2.4\ A\ cm^{-2}$. (a) Entry region and (b) exit region.

This latter observation can be attributed to the local temperature distribution at the membrane–cathode GDL interface. Specifically, as shown in Fig. 16, the local temperature increases significantly for Ch/Sh = 4 at $I_{avg} = 2.4\ A\ cm^{-2}$, and this higher temperature will lead to increases in the aop and cop of the cell (see Fig. 14b).

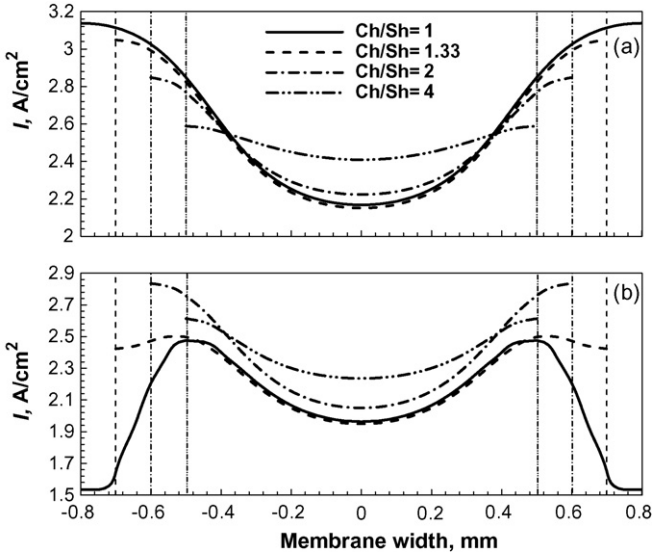

Fig. 15. Comparison of local current density distribution for different channel–shoulder width ratios for $I_{avg} = 2.4\ A\ cm^{-2}$. (a) Inlet region and (b) exit region.

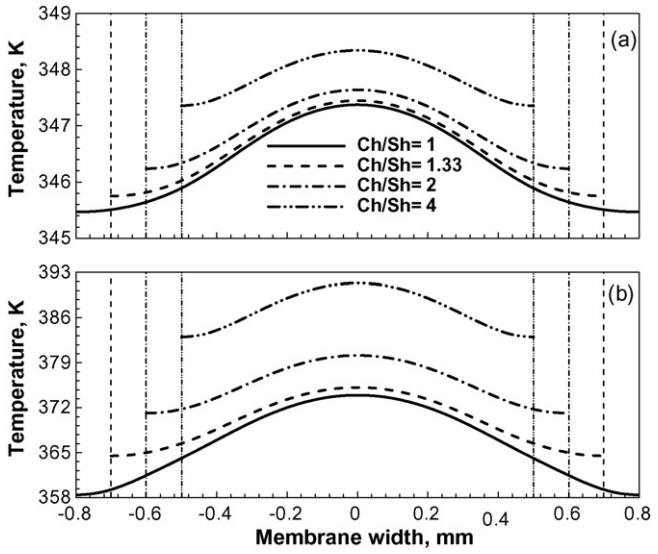

Fig. 16. Comparison of temperature distribution at the exit region for different channel–shoulder width ratios. (a) $I_{avg} = 0.6\ A\ cm^{-2}$ and (b) $I_{avg} = 2.4\ A\ cm^{-2}$.

Fig. 17 shows the oxygen mole fraction and membrane conductivity for different channel–shoulder width ratios at the channel exit region. Reducing the shoulder width usually improves the oxygen availability at the reacting area because the reactants need to travel a shorter distance. This provides more uniform reaction in the fuel cell and, as a consequence, the membrane conductivity decreases significantly as the channel–shoulder width ratio is increased. A higher oxygen mole fraction at the shoulder region helps to reduce the cop; however, lower membrane conductivity increases the Ohmic loss. The present simulation results indicate that the membrane conductivity plays a major role in voltage losses at high current density operation for higher channel–shoulder width ratios.

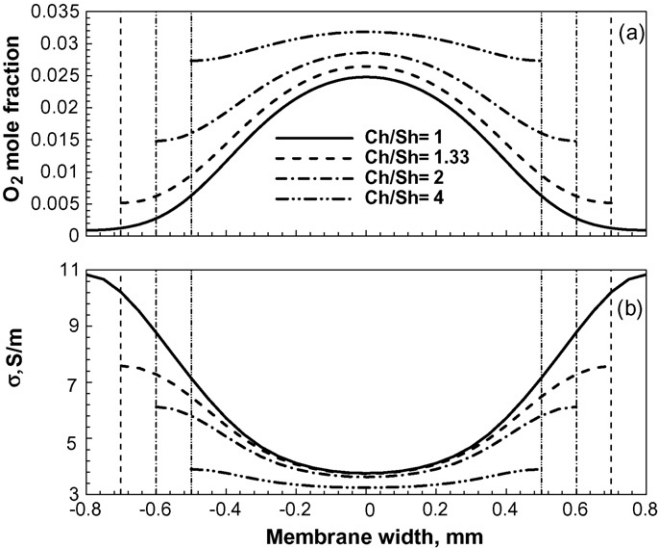

Fig. 17. Comparison of (a) oxygen mole fraction and (b) membrane conductivity distribution at the exit region for different channel–shoulder width ratios at $I_{avg} = 2.4\ A\ cm^{-2}$.

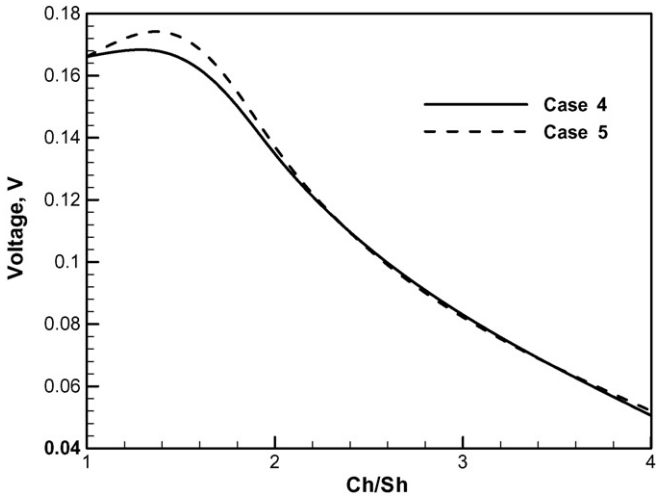

Fig. 18. Comparison of the cell voltage at $I_{avg} = 2.4\ A\ cm^{-2}$ for Cases 4 and 5.

3.3. Channel–shoulder width ratio with the same boundary conditions

Above we examined the cell performance as a function of channel–shoulder width ratio for systems in which the reactant inlet velocities were defined by Eq. (1). We now examine the performances of cells with different channel–shoulder width ratios (Case 5) but with the same boundary conditions (reactant mass flow rates and inlet boundary conditions). The boundary conditions for the base case (Case 1), which is the same as Cases 4.1 and 5.1, are used for the other sub-cases (Case 5.2, 5.3 and 5.4). When the boundary conditions are kept constant in this way, cells with a higher channel–shoulder width ratio (e.g., Case 5.4) will have larger quantities of reactants and inlet velocities at a given operating current density. Fig. 18 shows the cell voltage as a function of the channel–shoulder width ratio for Cases 4 and 5 at an operating current density of $2.4\ A\ cm^{-2}$. The cell voltage increases significantly at the optimum channel–shoulder width ratio for Case 5. At $I_{avg} = 2.4\ A\ cm^{-2}$, the cell voltages for Cases 4 and 5 are almost the same for channel–shoulder width ratios above Ch/Sh = 2. The different voltage losses (aop, cop and Ohmic loss) in the cell for this high operating current density are shown in Fig. 19. Comparing Figs. 14 and 19, the cop decreases significantly for Case 5 because higher amounts of reactants are flowing through the channels. However, compared to Case 4, the Ohmic loss in Case 5 increases to a much greater degree at higher channel–shoulder width ratios because of the lower membrane conductivity. Whereas for Case 4 there was no significant difference in cop between Ch/Sh = 2 and 4 (Fig. 14), for Case 5 the cop decreases slightly on going from Ch/Sh = 2–4 due to the higher amounts of reactants introduced through the channels at the same inlet temperature. The temperature distributions for Ch/Sh = 4 for Cases 4 and 5 are shown in Fig. 20. It is clear that the temperature distribution in the membrane–cathode GDL interface is lower for Case 5 than for Case 4, which will help to keep a low cop for the Case 5. Temperature starts to play a critical role on fuel cell performance at high operating current densities for higher channel–shoulder width ratio. PEMFC

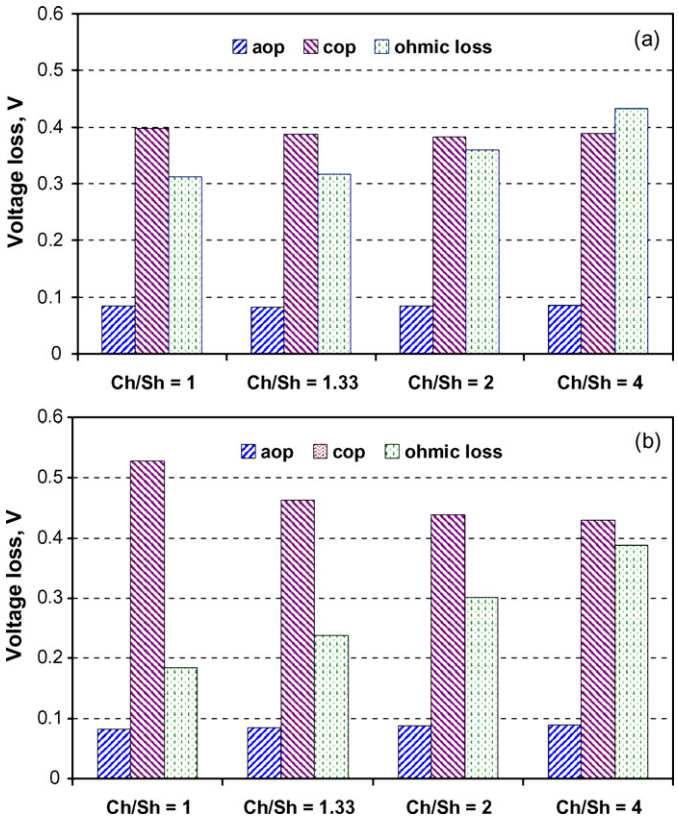

Fig. 19. Comparison of different voltage losses for $I_{avg} = 2.4$ A cm^{-2} by keeping the same boundary conditions for all shoulder widths. (a) Entry region and (b) exit region.

with better cooling systems like using air holes (for sub kW systems) or water holes through the bipolar plates can be considered to obtain uniform temperature distribution in the cell. The uniform temperature distribution will enhance the cell performance by improving the anode water activity, membrane conductivity and will reduce the different thermal expansions and thermal stresses of the membrane, GDL and bipolar materials. However, the membrane conductivity is found to be a main determinant of Ohmic loss and was shown to be a major factor influencing the total voltage losses for higher channel–shoulder width ratios at high current density operation.

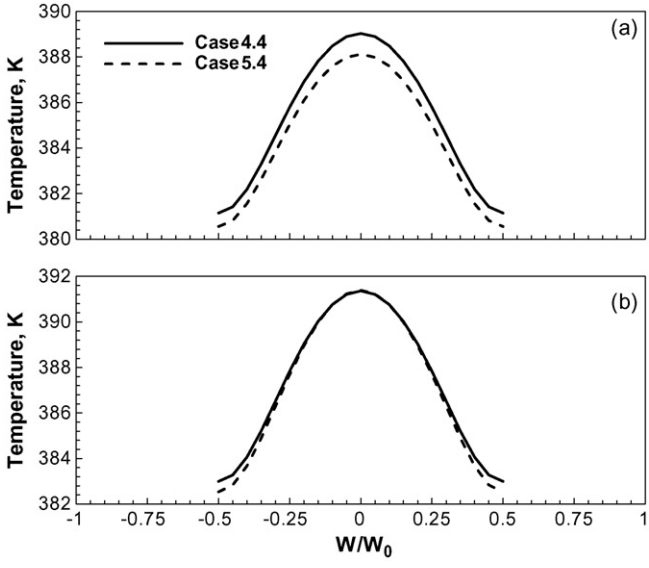

Fig. 20. Comparison of temperature distributions of Cases 4 and 5 for Ch/Sh = 4. (a) Entry region and (b) exit region.

4. Conclusions

In the present study, we carried out simulations of a PEMFC with a single straight channel geometry. The main aim of this work was to examine the cell performance at high operating current density of cells with different geometric configurations but the same boundary conditions. First, three different channel cross-sections (rectangular, trapezoidal and parallelogram) were chosen with the same channel height, channel area and reacting area, which ensured the same boundary conditions for all cases. The results of simulations using these channel geometries revealed that the rectangular channel cross-section gave higher cell voltages, but the trapezoidal channel cross-section gave more uniform reactant and local current density distributions at the membrane–cathode GDL interface. Moreover, the results indicated that the cathode overpotential and Ohmic loss were particularly sensitive to the shoulder width. We therefore performed simulations of cells with a rectangular channel cross-section and various shoulder widths, and found that the cell voltage was insensitive to the shoulder width for current densities in the low range. At high operating current density, by contrast, there was an optimum channel–shoulder width ratio (Ch/Sh = 1.3–1.4). The cell performance deteriorated at higher channel–shoulder width ratios, especially at high operating current density. Channels with smaller shoulder widths exhibited higher oxygen concentration and local current density, but significantly lower membrane conductivity because of their lower anode water activity. As a consequence, the cop decreases and the Ohmic loss increases in the fuel cell for high operating current density. The modeling was repeated so as to examine the variation in cell performance when the same boundary conditions were maintained for different channel–shoulder width ratios. The results revealed the presence of an optimum channel–shoulder ratio, at which the cell performance increases significantly for high operating current density compared with other channel–shoulder width ratios. The membrane conductivity and shoulder width were found to be very influential physical and geometrical parameters, respectively, that regulated the Ohmic loss and overall cell performance under high current density operation.

Acknowledgment

This work was supported by the Brain Korea 21 Project in 2006.

References

[1] E.A. Ticianelli, C.R. Derouin, S. Srinivasan, J. Electroanal. Chem. 251 (1988) 275–295.

[2] J.H. Wee, Applications of proton exchange membrane fuel cell systems, Renewable Sustainable Energy Rev., in press.
[3] J. Larminie, A. Dicks, Fuel Cell Systems Explained, second ed., Wiely, England, 2003, pp. 51–52.
[4] P. Costamagna, Chem. Eng. Sci. 56 (2001) 323–332.
[5] T.E. Springer, M.S. Wilson, S. Gottesfeld, J. Electrochem. Soc. 140 (12) (1993) 3513–3526.
[6] V. Garau, H. Liu, S. Kakac, AIChE J. 44 (11) (1998) 2410–2422.
[7] S. Dutta, S. Shimpalee, J.W. Van Zee, Int. J. Heat Mass Transfer 44 (2001) 2029–2042.
[8] D. Natarajan, T.V. Nguyen, J. Electrochem. Soc. 148 (12) (2001) A1324–A1335.
[9] K.W. Lum, J.J. McGuirk, J. Electrochem. Soc. 152 (4) (2005) A811–A817.
[10] U. Pasagullari, C.Y. Wang, J. Electrochem. Soc. 152 (2) (2005) A380–A390.
[11] A. Kumar, R.G. Reddy, J. Power Sources 113 (2003) 11–18.
[12] G. Lin, T.V. Nguyen, J. Electrochem. Soc. 153 (2) (2006) A372–A382.
[13] G.H. Guvelioglu, H.G. Stenger, J. Power Sources 147 (2005) 95–106.
[14] K.W. Lum, J.J. McGuirk, J. Power Sources 143 (2005) 103–124.
[15] D. Natarajan, T.V. Nguyen, J. Power Sources 115 (2003) 66–80.
[16] W. Sun, B.A. Peppley, K. Karan, J. Power Sources 144 (2005) 42–53.
[17] M.S. Chiang, H.S. Chu, Numerical investigation of transport component design effect on a proton exchange membrane fuel cell, J. Power Sources, in press.
[18] L. Sun, P.H. Oosthuizen, K.B. McAuley, A numerical study of channel-to-channel flow cross-over through the gas diffusion layer in a PEM-fuel-cell flow system using a serpentine channel with a trapezoidal cross-sectional shape, Int. J. Therm. Sci., in press.
[19] H.M. Jung, W.Y. Lee, J.S. Park, C.S. Kim, Int. J. Hydrogen Energy 29 (2004) 945–954.
[20] W.K. Lee, S. Shimpalee, J.W. Van Zee, J. Electrochem. Soc. 150 (3) (2003) A341–A348.
[21] J.J. Hwang, C.K. Chen, R.F. Savinell, C.C. Liu, J. Wainright, J. Appl. Electrochem. 34 (2004) 217–224.
[22] F.B. Weng, A. Su, G.B. Jung, Y.C. Chiu, S.H. Chan, J. Power Sources 145 (2005) 546–554.
[23] A. Su, Y.C. Chiu, F.B. Weng, Int. J. Energy Res. 29 (2005) 409–425.
[24] S. Shimpalee, W.K. Lee, J.W. Van Zee, H.N. Neshat, Predicting the transient response of a serpentine flow-field PEMFC I. Excess of normal fuel and air, J. Power Sources 156 (2) (2006) 355–368.
[25] Y. Wang, C.Y. Wang, J. Power Sources 147 (2005) 148–161.
[26] W. Ying, Y.J. Sohn, W.Y. Lee, J. Ke, C.S. Kim, J. Power Sources 145 (2005) 563–571.
[27] W. Ying, T.H. Yang, W.Y. Lee, J. Ke, C.S. Kim, J. Power Sources 145 (2005) 572–581.
[28] W.Q. Tao, C.H. Min, X.L. Liu, Y.L. He, B.H. Yin, W. Jiang, Parameter sensitivity examination and discussion of PEM fuel cell simulation model validation part 1. Current status of modeling research and model development, J. Power Sources, in press.
[29] C.H. Min, Y.L. He, X.L. Liu, B.H. Yin, W. Jiang, W.Q. Tao, Parameter sensitivity examination and discussion of PEM fuel cell simulation model validation part 2. Results of sensitivity analysis and validation of the model, J. Power Sources, in press.
[30] L. Wang, A. Husar, T. Zhou, H. Liu, Int. J. Hydrogen Energy 28 (2003) 1263–1272.
[31] C.R. Tsai, F. Chen, A.C. Ruo, M.H. Chang, H.S. Chu, C.Y. Soong, W.M. Yan, C.H. Cheng, An analytical solution for transport of oxygen in cathode gas diffusion layer of PEMFC, J. Power Sources, in press.
[32] D.M. Bernardi, M.W. Verbrugge, J. Electrochem. Soc. 139 (9) (1992) 2477–2491.
[33] S. Um, C.-Y. Wang, K.S. Chen, J. Electrochem. Soc. 147 (12) (2000) 4485–4493.
[34] P.T. Nguyen, T. Berning, N. Djilali, J. Power Sources 130 (2004) 149–157.
[35] T.E. Springer, T.A. Zawodzinski, S. Gottesfeld, J. Electrochem. Soc. 138 (8) (1991) 2334–2342.
[36] J.C. Slattery, R.B. Bird, AIChE J. 4 (1958) 137–142.
[37] S. Dutta, S. Shimpalee, J.W. Van Zee, J. Appl. Electrochem. 30 (2000) 135–146.
[38] STAR-CD Version 3.24 Methodology, CD-Adapco Group.
[39] B. Cheng, O. Minggao, Y. Baolian, J. Tsinghua Sci. Technol. 11 (1) (2006) 54–64.
[40] D. Singh, D.M. Lu, N. Djilali, Int. J. Eng. Sci. 37 (1999) 431–452.
[41] T.F. Fuller, J. Newman, J. Electrochem. Soc. 140 (5) (1993) 1218–1225.
[42] S. Shimpalee, S. Dutta, Num. Heat Transfer, Part A 38 (2000) 111–128.